Deep structure of the Alborz Mountains by joint inversion of P receiver functions and dispersion curves

Mehdi Rastgoo[a], Habib Rahimi[a,*], Khalil Motaghi[b], Esmaeil Shabanian[b], Fabio Romanelli[c], Giuliano F. Panza[d,e,f]

[a] Institute of Geophysics, University of Tehran, Tehran, Iran
[b] Institute for Advanced Studies in Basic Sciences, 45195-1159 Zanjan, Iran
[c] Department of Mathematics and Geosciences, University of Trieste, Trieste, Italy
[d] Accademia Nazionale dei Lincei, Roma, Italy
[e] Institute of Geophysics, China Earthquake Administration, Beijing, China
[f] International Seismic Safety Organization (ISSO), Italy

ARTICLE INFO

Keywords:
Delamination
Alborz Mountains
Velocity model
Receiver function
Dispersion data

ABSTRACT

The Alborz Mountains represent a tectonically and seismically active convergent boundary in the Arabia – Eurasia collision zone, in western Asia. The orogenic belt has undergone a long-lasted tectono-magmatic history since the Cretaceous. The relationship between shallow and deep structures in this complex tectonic domain is not straightforward. We present a 2D velocity model constructed by the assemblage of 1D shear wave velocity (Vs) models from 26 seismic stations, mainly distributed along the southern flank of the Alborz Mountains. The shear wave velocity structure has been estimated beneath each station using joint inversion of P-waves receiver functions and Rayleigh wave dispersion curves. A substantiation of the Vs inversion results sits on the modeling of Bouguer gravity anomaly data. Our velocity and density models show low velocity/density anomalies in uppermost mantle of western and central Alborz at a depth range of ~50–100 km. In deeper parts of the uppermost mantle (depth range of 100–150 km), a high velocity/density anomaly is located beneath most of the Mountain range. The spatial pattern of these low and high velocity/density structures in the upper mantle is interpreted as the result of post collisional delamination of lower part of the western and central Alborz lithosphere.

1. Introduction

The Iranian plateau is located between the Arabian and Eurasian plates that converge at a rate of ~15–26 mm/yr (Vernant et al., 2004). This convergence is partly accommodated by folding and thrust faulting in the Zagros mountain belt at the southwest margin of the Iranian plateau and in the Alborz and Kopeh Dagh mountains in the north and northeast (Fig. 1). The Alborz Mountains is a relatively narrow V shaped deformation belt, trapped between the central Iranian microplate to the south and the rigid South Caspian Basin to the north. Tectonic activity of Alborz results from the interaction of these two tectonic domains which, involved in the active convergence, are characterized by distinct rheologies and relative motions (e.g., Ritz et al., 2006; Shabanian et al., 2012 – Fig. 1). The relative motion between Central Iran and the South Caspian Basin is accommodated in different ways in the V shaped Alborz belt (see Shabanian et al., 2012 and references therein for a review). The analysis of a dense network of GPS sites covering Central Alborz (Djamour et al., 2010) has revealed important kinematic aspects of the present-day deformation. For the faults south of the range (Mosha, Firuzkuh, and Astaneh), the vertical component of faulting is not significant, consistent with the fact that the faults are mainly left-lateral (e.g., Hedayati et al., 1976; Trifonov et al., 1996; Jackson et al., 2002; Allen et al., 2003; Hessami et al., 2003; Ashtari et al., 2005; Nemati et al., 2011; Solaymani Azad et al., 2011). At the northern border, the Khazar Fault which is suggested as the tectonic boundary between Alborz and the South Caspian Basin (e.g., Berberian et al., 1983), is divided into two distinct portions: (1) the western segment is mainly a thrust fault slipping at ~6 mm/yr, with a left-lateral component of ~2–3 mm/yr; (2) the eastern segment is predominately left-lateral (~5 mm/yr) accompanied with a lesser component of thrust faulting at ~2–3 mm/yr. The obliquity of the South Caspian Block relative to Central Iran varies from ~25° in the

* Corresponding author.
E-mail address: rahimih@ut.ac.ir (H. Rahimi).
URL: http://www.issoquake.org (G.F. Panza).

Accepted 17 January 2018

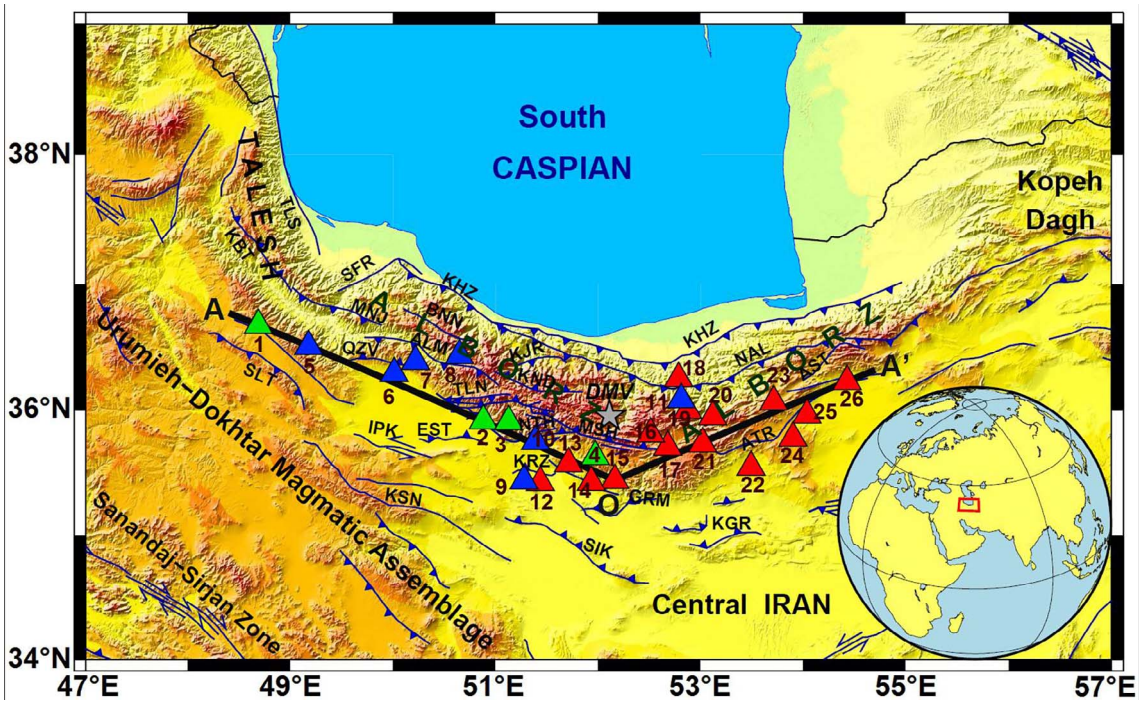

Fig. 1. Study region with the locations of the 26 seismic stations along AOA' profile, marked by triangles. Red triangles represent the locations of temporary seismic stations installed by IIEES; green triangles represent the locations of permanent stations installed by IIEES; blue triangles represent the locations of permanent stations installed by IGUT. DMV: Damavand volcano, KHZ: Khazar fault, NAL: North Alborz fault, MNJ: Manjil fault, QZV: Qazvin fault, ALM: Alamut fault, TLN: Taleqan fault, KND: Kandovan fault, AST: Astaneh fault, ATR: Atari fault, KGR: kuh gugerd fault, SIK: Siah kuh fault, GRM: Garmsar fault, MSH: Mosha fault, KJR: Kojour fault, NTH: North Tehran fault, KRZ: Kahrizak fault, BNN: Banan fault, EST: Eshtehard fault, KSN: Kushk Nosrat fault, IPK: Ipak fault, SFR: Sefidrud fault, KBT: Kabateh fault, SLT: Soltaniyeh fault, TLS: Talesh fault. Based on the slip rate study performed by Panahi Vaghar et al. (2017), slip rate of KHZ is 1.2 mm/yr along its strike and 0.3 mm/yr along its dip; slip rate of NAL is 0.1 mm/yr along its strike and 0.6 mm/yr along its dip; slip rate of MNJ is 0.1 mm/yr along its strike and 0.7 mm/yr along its dip; slip rate of QZV is 1.1 mm/yr along its strike and 0.9 mm/yr along its dip; slip rate of ALM is 0.1 mm/yr along its strike and 0.7 mm/yr along its dip; slip rate of TLN fault is 0.4 mm/yr along its strike and 1.8 mm/yr along its dip; slip rate of KND is 1.7 mm/yr along its strike and 0.2 mm/yr along its dip; slip rate of AST is 1.2 mm/yr along its strike and 1.7 mm/yr along its dip. (For interpretation of the references to colour in this figure legend, the reader is referred to the web version of this article.)

western part of Central Alborz to ~70° in the eastern part of the range (Djamour et al., 2010). These observations imply that the eastern part of Central Alborz principally accommodates strike-slip deformation, while the western part of Central Alborz takes up compressional deformation by thrust faulting and shortening (see Shabanian et al., 2012 and references therein). Such a tectonic configuration implies a thickened lithosphere that includes a thick crust beneath, at least, the central to western portion of the Alborz belt.

The Alborz Mountains has a relatively high topography (see Radjaee et al., 2010; Shabanian et al., 2012) and include several peaks with elevation between 3600 and 4800 m, among which Mt. Damavand (5671 m) is the highest. Dehghani and Makris (1984) showed that the gravity field along the Alborz Mountains, in spite of the relatively high topography, reaches small negative values. This clearly represents an undercompensated isostatic situation which normally should result in significant subsidence in the belt, while the Alborz Mountains is still uplifting.

During the last decade, several geophysical investigations have been carried out to explain this discrepancy. Using P and S wave receiver functions technique, Sodoudi et al. (2009) reported Moho depths of 51–54 km and lithospheric thickness of ~90 km beneath the central part of Alborz. Radjaee et al. (2010), using joint inversion of receiver functions and surface waves, have estimated Moho depths of 55–58 km below the central part of Alborz (longitudes of 51.2°E to 52.3°E), and ~46 km beneath the coastal region of the South Caspian basin to the north. Rahimi et al. (2014) have used surface wave dispersion curves to reconstruct shear wave velocity structures in different part of the Iranian plateau. The respective average crustal and lithospheric thicknesses of ~46 km and ~120 km were reported for the Alborz region. Rahimi et al. (2014) proposed that the Alborz has a thin lithosphere with a thin to moderate thickness crust unable to compensate the high topography of the Mountain range (see also Radjaee et al., 2010). Despite our increasing knowledge on this issue, the main geodynamic questions remain unanswered: what geodynamic process is behind the abnormal uprise of the Mountain range and how it is controlling the active topography of the belt?

This paper presents original data and interpretations to resolve deep structures of the Alborz Mountains in order to (1) characterize spatial variations in the velocity structure of the lithosphere beneath Alborz, and (2) to propose a geodynamic model that explains the variations in accordance with both topography and tectonic structure of the belt. We have calculated shear wave velocity structure of the region based on the joint inversion of P receiver functions and Rayleigh wave group velocity dispersion data (Julia et al., 2000). P receiver functions have been initially calculated beneath 26 seismic stations and then 1D shear wave velocity (Vs) distribution with depth has been estimated beneath each station using the joint inversion procedure. We juxtapose 26 obtained 1-D velocity models to construct a 2-D S-wave velocity model along the seismic profile (line AOA' in Fig. 1). The obtained resolution of the lateral variability of the lithosphere–asthenosphere system is substantiated by the Bouguer gravity anomaly along the profile: starting from a density model obtained from the Vs model, via a standard

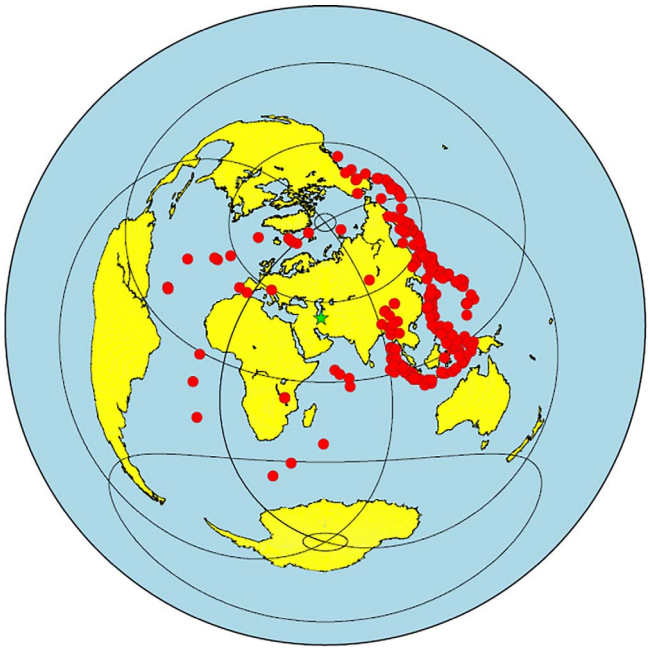

Fig. 2. Azimuthal distribution of the 323 teleseismic earthquakes (red circles), with epicentral distance between 30° and 95° from Alborz region (Green star), considered in this study. These events have been recorded from February 2009 till September 2014 and have magnitude Mw > 5.4 (USGS catalog, 2015). (For interpretation of the references to colour in this figure legend, the reader is referred to the web version of this article.)

relation between density and Vs (e.g. Ludwig et al., 1970). The density distribution beneath the seismic profile is determined by linear inversion of Bouguer anomaly. The spatial variations of Moho and lithosphere-asthenosphere boundary, as well as the spatial variations of shear wave velocity and density resolved by this procedure, are interpreted in terms of regional-scale geodynamic processes.

2. Data preparation

Teleseismic body waveforms have been used to compute P Receiver Functions (PRF), which are sensitive to major seismic discontinuities inside the Earth crust and uppermost mantle. In this study, we selected 323 teleseismic events recorded between February 2009 and September 2014 (Fig. 2). The events had moment magnitude of 5.5 or greater and epicentral distance of 30°-95°. Fifteen stations (red triangles, Fig. 1) are temporary stations, operated by the International Institute of Earthquake Engineering and Seismology (IIEES) from October 2009 to November 2010. We added 4 permanent broadband stations of IIEES (green triangles in Fig. 1) and 7 permanent broad-band and short period seismic stations of Institute of Geophysics, University of Tehran (blue triangles in Fig. 1) to expand the study area.

To calculate PRFs, the teleseismic P waveforms were cut from 60 s before to 120 s after the theoretical P wave onset. ZNE-component waveforms were rotated into the ZRT coordinate system and the Z component was deconvolved from the R component using the iterative deconvolution method of Ligorria and Ammon (1999). The Gaussian smoothing factor of 1.0 (equivalent to a 0.5 Hz low pass filter) was applied to the PRFs to smooth small-scale features and remove high frequency noise. The obtained PRFs are naturally source–station distance dependent and to overcome this fact a simple moveout correction (Kind and Vinnik, 1988; Zhu and Kanamori, 2000; Motaghi et al., 2012) was used. The PRFs from different back-azimuths were stacked and the standard deviation of stacking was considered as the error bar for stacked PRF at each station. Fig. 3(a–e) shows the stacked and individual moveout corrected PRFs, calculated for stations HSB1, ZNJK, DAMV, ALA1 and AHM1. The location of these stations is shown in Fig. 1 by numbers 9, 1, 4, 11 and 15, respectively. Rayleigh wave group velocity dispersion curves have been extracted from the surface wave tomographic maps calculated by Rahimi et al. (2014) with a resolution of about $0.5^\circ \times 0.5^\circ$. For each station, Rayleigh wave dispersion data were extracted from the relevant cell containing that station.

3. Joint inversion procedure

Surface wave dispersion curves are sensitive to absolute S-wave velocity while PRFs provide constraints on major velocity discontinuities such as Moho boundary. The merits of the joint inversion using both datasets have been discussed in numerous previous studies (e.g. Julia et al., 2000). In this study, we follow the joint inversion procedure described by Motaghi et al. (2015, 2017) and only a brief outline of the method is presented here. The inversion program is "joint96" which is available in the software package 'Computer Programs in Seismology' (Herrmann, 2013). It uses damped least squares method (Menke, 1989) to invert the two data sets for an S-wave velocity model.

The joint inversion is based on the linearization of a non-linear inversion problem; therefore, the final model is critically dependent on the initial model (starting model used in the inversion process). The use of reliable initial models obtained from independent studies can minimize this intrinsic drawback (e.g. Gonzalez et al., 2012; Motaghi et al., 2015; Last et al., 1997). When an appropriate initial model can be generated using a priori information, linearized inversions can find an optimal solution that is the global minimum of a misfit function. The initial models used in this study (Fig. 4) are taken from Rahimi et al. (2014) who have presented a set of shear wave velocity models for each main tectonic region of Iran (e.g. Alborz and Zagros) employing the hedgehog non-linear inversion (Panza, 1981) of the average dispersion curves for each tectonic region. The average dispersion curves are obtained averaging all dispersion curves calculated for each tectonic region.

The iteration process in the joint inversion process is terminated when the variation of the percent of fit is less than 0.05. This controlling parameter is defined as the percent of fit between the theoretical and experimental receiver functions. When the inversion is terminated, the corresponding model is regarded as an output model. The repetition of the iterative procedure for a set of initial models results in a set of output models for each station. To summarize and interpret the results, a representative model for each station is chosen based on the following criterion: It is the output model that has the closest percentage of fit to the average value of all percentages of fits obtained from all the solutions for the station. This criterion reduces the effects of the projection of possible systematic errors into the inverted structural model (e.g. Motaghi et al., 2017). The maximum depth of effective penetration is about 300 km, accordingly with the depth resolution of the dataset, determined using the partial derivatives (Urban et al., 1993) of the dispersion curves with respect to the shear wave velocity distribution versus depth.

To find the most robust final velocity model for each station, the following regularizations have been introduced: 1) search for the optimal parameterization for the inversion process; and 2) simplification of the representative model (Motaghi et al., 2015). To find the optimum parameterization, the incremental step (IS) is defined as the minimum resolvable layer thickness by the dispersion data (Panza, 1981). This parameter has been used in the non-linear inversion of dispersion data and reported by Rahimi et al. (2014) for dispersion data in each tectonic region. In the joint inversion procedure, four different

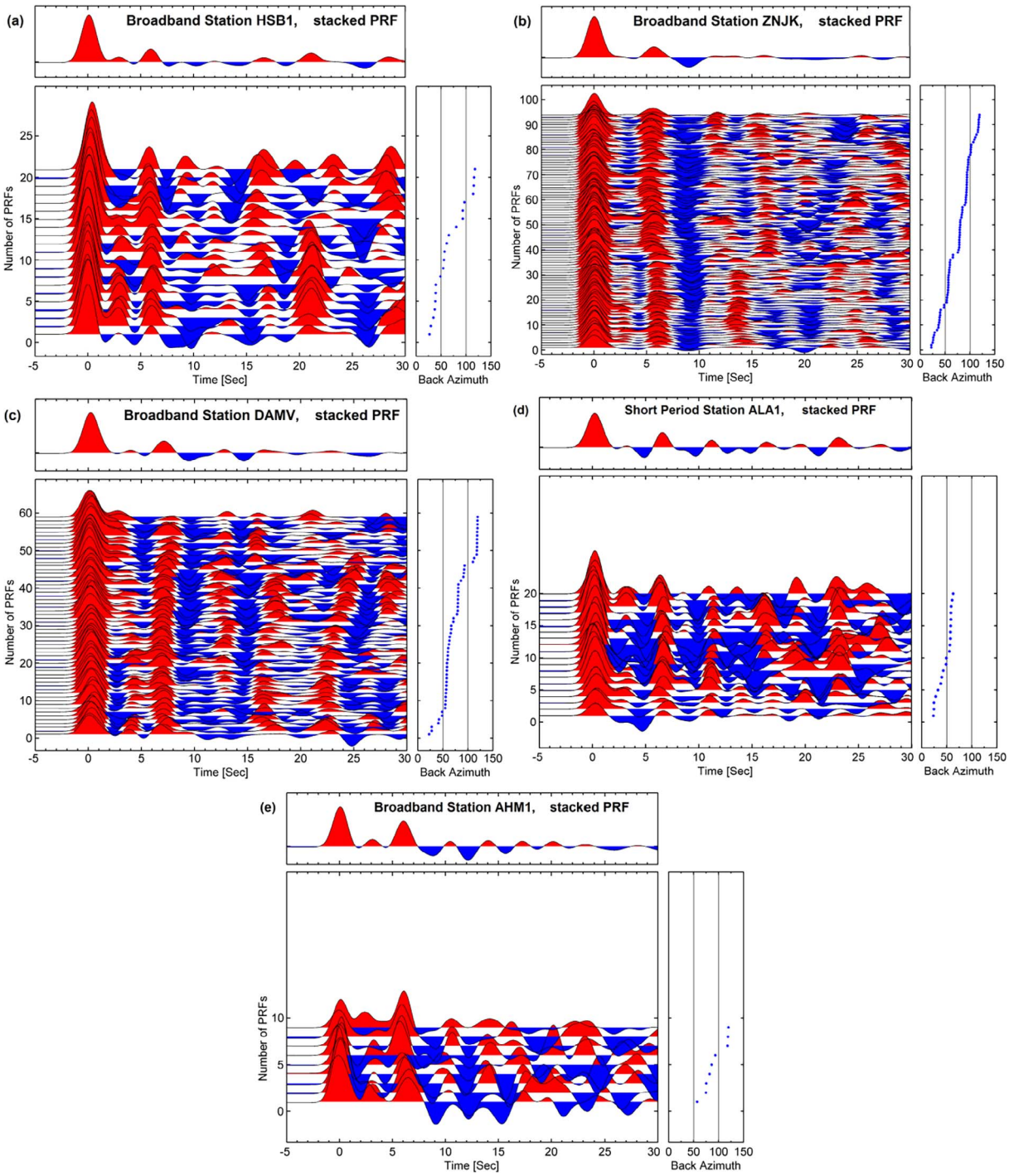

Fig. 3. Individual and stacked PRFs for stations: HSB1(a), ZNJK (b), DAMV (c), ALA1 (d) and AHM1 (e) (numbered by 9, 1, 4, 11 and 15, respectively, in Fig. 1). The traces are arranged with increasing back azimuth (blue dots). (For interpretation of the references to colour in this figure legend, the reader is referred to the web version of this article.)

parameterizations were tried by subdividing each layer of the initial models in sub-layers with thickness equal to IS/1, IS/1.25, IS/1.5 and IS/2. If the layer subdivision improves the fit between the theoretical and experimental receiver functions ($> 1\%$), the new parameterization will be accepted. Otherwise the simpler model is considered as the final model (Motaghi et al., 2015). Uncertainties for discontinuity depths (e.g. Moho depth) are defined as $\pm$ half of the parameter's step at that depth (i.e., equal half of minimum thickness, found by optimizing parameterization). Fig. 5 shows the final models obtained for the four parameterizations (IS/1, IS/1.25, IS/1.5 and IS/2) for HSB1 station. The representative model is simplified reducing the number of different layers. The main velocity contrasts are recognized and the average velocity of the layers located between those assumed boundaries is calculated. For the simplified model, the theoretical PRF and dispersion curve are computed using forward modeling. If these theoretical curves fall within the experimental error bars, the simplified model is regarded

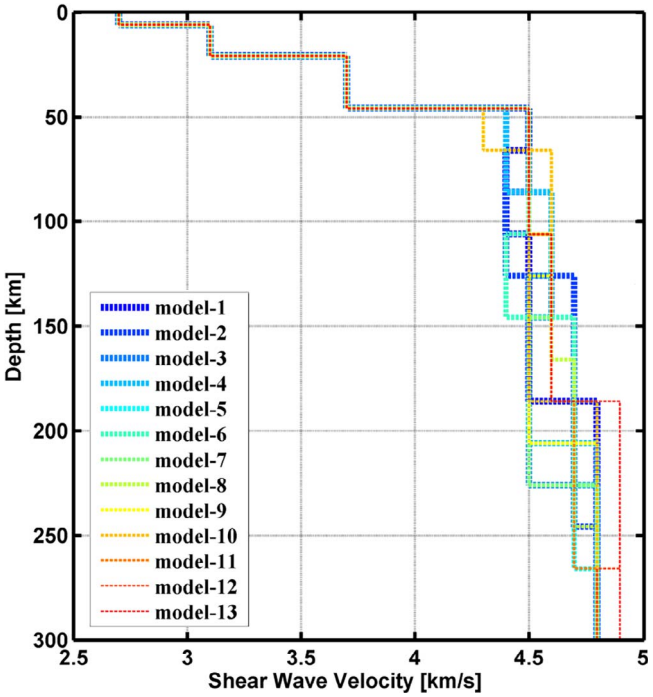

Fig. 4. Set of shear wave velocity models for the Alborz region (taken from Rahimi et al., 2014), used as initial models in this study.

as the final model. Otherwise more details will be added by considering more layers in the simplified model. Fig. 6 shows examples of the joint inversion results corresponding to appropriate parameterization and smoothing of the representative model for c (numbers 9, 1, 4, 11 and 15, respectively in Fig. 1).

Fig. 7 shows the resolution kernels calculated for the final velocity model of HSB1. In this figure, red lines represent the normalized values of each column of the resolution matrix. Theoretically, the resolution matrix is an identity matrix if all inverted parameters are not cross-correlated. In practice, due to the unavoidable correlation, if the model is satisfactorily resolved, it is a matrix with narrow peaks occurring near the main diagonal. This matrix shows that the estimated model parameters turn out to be linear combinations of the correlated true model parameters (Menke, 1989). For all of the stations, the resolution kernels were computed (Table 1). We limited the maximum depth of investigation to 300 km (Fig. 7) because the longest available period of the group velocity dispersion curve is 100 s, i.e., surface waves sample to a depth less than 350 km, and also the resolution kernels (obtained for all stations) show that the average depth of resolvable features are not deeper than 300 km. According to Fig. 7, the representative model of HSB1 station has 24 layers (left panel) and the right panel shows that the layer number 20, corresponding to depth range 238–350 km, centered in 294 km, is the deepest layer can detect the features. Table 1 gives the maximum depth of the resolvable features that are obtained from resolution kernels for each seismic station. Furthermore, the estimated Moho depth values beneath each seismic station are presented in this table. The shallow sharp low-to-high (Vs $>$ 4.0 km/s) velocity contrast in the velocity models is conventionally considered as the Moho boundary (e.g. boundary at $\sim$50 km depth in Fig. 6-right panel).

To construct a 2D S-wave velocity model (Fig. 8), we combined the simplified 1D velocity models. The assembled 2D model is made up of several 20 km-wide blocks, each containing a number of stations. A 1D velocity model was assigned to each block by taking the average of the velocity models derived from the stations falling into the block. The blocky model was then smoothed using Gaussian filter. The 2D velocity model obtained in such a way has been used as a priori constraint to generate a 2D density model by inversion of Bouguer gravity anomaly, as described in Section 4.

4. Independent geophysical constraint: Gravity modeling

The complexity of the Earth structure and the epistemic limit in its study, which is mainly related to the limited capability of direct measurement of its physical properties, request a multidisciplinary approach to constrain geophysical modeling based on independent geophysical data from different fields. The measurement of the gravimetric field is very useful in this respect. We used the geometry of the velocity models obtained in Section 3 (see Fig. 8) as a priori constraints (initial model) for the linear inversion of gravity Bouguer anomaly data to density distribution. Based on the Nafe–Drake relation (Ludwig et al., 1970), density is related to the seismic velocity with some uncertainty. The error band of the Nafe–Drake relation is about $\pm$ 0.20g/cm^3 in the crust (density $<$ 3.00g/cm^3) and about $\pm$ 0.22g/cm^3 for the upper mantle (density $>$ 3.20g/cm^3). The density anomaly can be computed by subtracting this density model from a reference density model which is defined as follows: density of 2.50 g/cm^3 for the upper 25 km, density of 2.70 g/cm^3 for 25–50 km, density of 3.20 g/cm^3 for 50–200 km and density of 3.60 g/cm^3 for 200–300 km of depth. The Bouguer anomaly is calculated using the density anomaly. Usually, the initial misfit between calculated and observed Bouguer anomaly is large and therefore the density value in each layer iteratively is modified within the error band of the Nafe–Drake relation. The smallest perturbation step is fixed at 0.05 g/cm^3, consistently with the resolving power of available data. The density perturbation is defined by the equation:

$$\rho_f = \rho_i \mp 0.05n\frac{g}{cm^3}$$

where ρ_i, ρ_f and n are the initial density, final density and the number of perturbation steps, respectively. Observed Bouguer anomaly data were extracted from the database of International Center for Global Earth Models (ICGEM), based on a global gravity model called GGM05C (Ries et al., 2016). Fig. 9 shows the density model (lower panel), which predicts a Bouguer anomaly (red squares in upper panel) well consistent with observed data (blue line in upper panel).

5. Results and discussion

In this study, the depths of Moho and LAB (Lithosphere Asthenosphere Boundary) beneath each station have been determined through 1D shear-wave velocity models (e.g. Fig. 6). No significant crustal thickness variation is observed along the seismic profile. Along the considered profile, the average crustal thickness beneath Alborz is $\sim$47 km (ranging from 42 to 50 km; Fig. 8). Sodoudi et al. (2009) and Radjaee, et al. (2010) reported 46–58 km crustal thickness beneath the Central Alborz. Chen et al. (2016) and Sobouti (As of yet unpublished result) reported 35–50 km crustal thickness beneath the western Alborz. The calculated crustal thickness along the Mountain range is not sufficient to compensate the average $\sim$2000 m elevation of the Alborz Mountains.

A clear expression of the seismic LAB is the decrease in Vs from high, in the lithospheric mantle, to low in the asthenosphere. The generalized occurrence of this velocity reduction is well established (e.g. Brune and Dorman, 1963; Dziewonski & Anderson, 1981). Such decrease could be found in 1D velocity models calculated for station HSB1 in eastern Alborz (Fig. 6a) revealing a lithospheric thickness of $\sim$170 km. In western and central Alborz, however, two low velocity features could be recognized in the uppermost mantle (Fig. 8). The

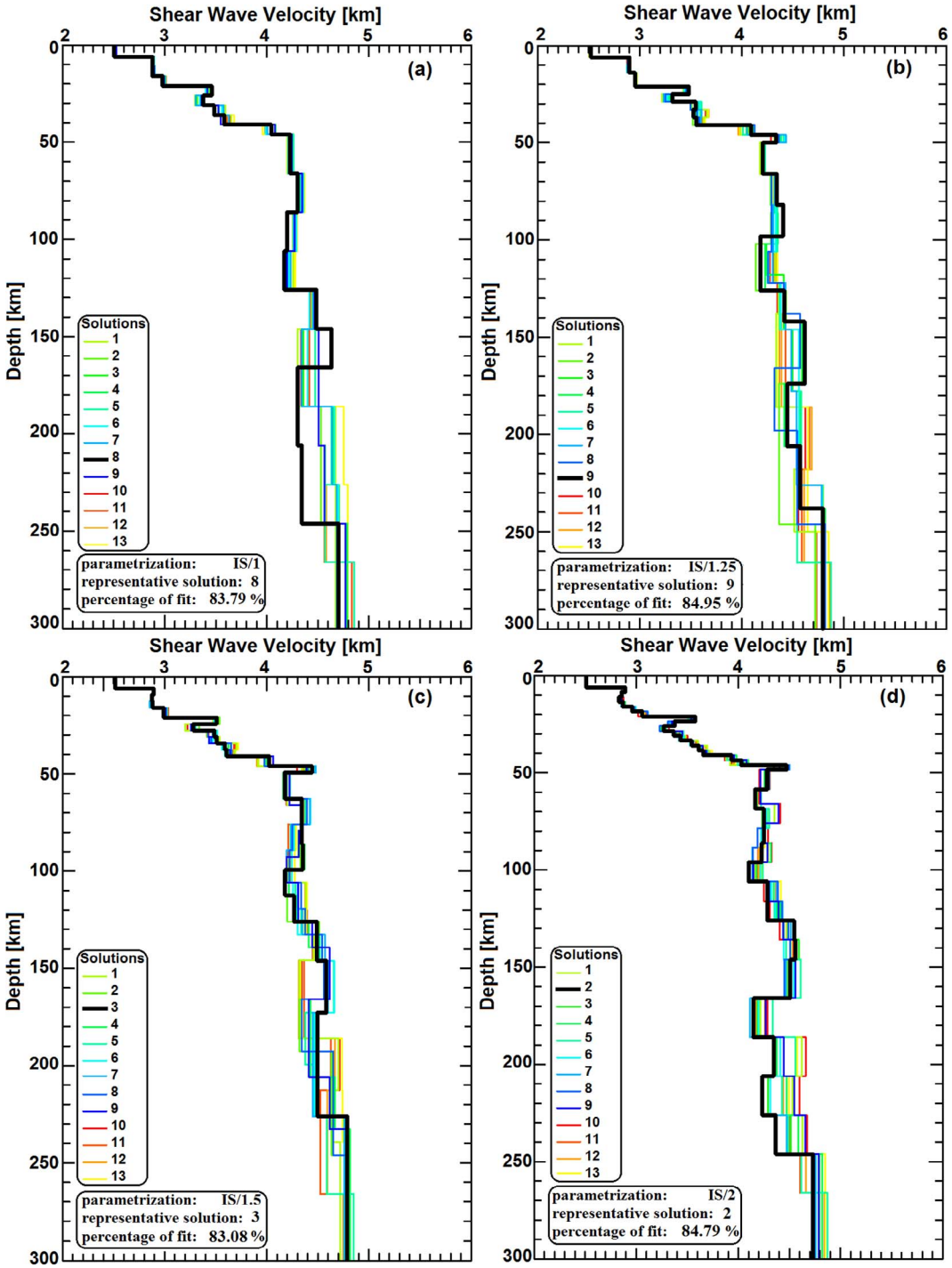

Fig. 5. Results of the first regularization test (four different parameterizations) for HSB1 station (station number 9 in Fig. 1). The thickness of inverted layers has been subdivided in sub-layers with thickness equal to: IS/1 (a), IS/1.25 (b), IS/1.5 (c) and IS/2 (d). In each case, the chosen solution is the one with the closest percentage of fit (between the theoretical and experimental receiver functions) to the average value of all percentages of fits obtained from all the solutions.

shallower one is centered at depth less than 100 km (e.g. 90 km for HSB1, Fig. 6a) and the deeper one starts at ~170 km similar to the depth for low velocity boundary in the eastern Alborz. A shallow low velocity boundary at depth of 90 km has been observed and reported before by S-wave receiver function technique in Central Alborz by Sodoudi et al. (2009) and was interpreted as bottom of a very thin lithosphere under the study area. Discrimination of the existing boundaries, as the base of the lithosphere beneath the western and central Alborz, is difficult and we talk about it later in accord to free-air gravity anomaly.

The S-wave velocity model reconstructed along the Alborz Mountains is shown in Fig. 8. The most significant velocity/density

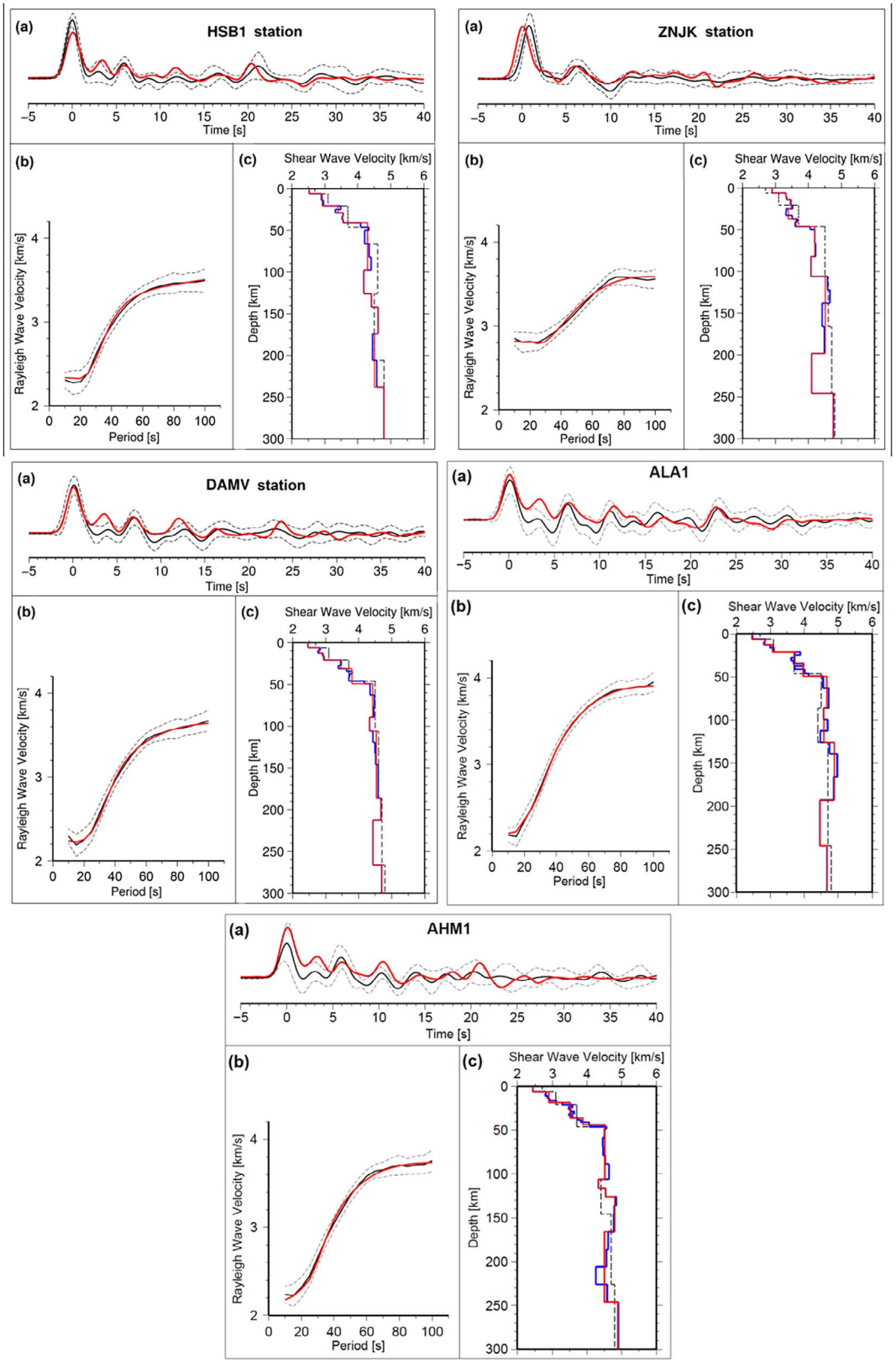

Fig. 6. Result of the joint inversion process and smoothing of the representative model for stations HSB1, ZNJK, DAMV, ALA1 and AHM (numbered as 9, 1, 4, 11 and 15, respectively, in Fig. 1). (a): experimental stacked PRF (black line), its error bar (black dashed lines) and theoretical PRF (red line) are computed from the smoothed model shown by red line in (c). (b): experimental group velocity (black line), its error bar (black dashed lines) and theoretical group velocity (red line) are computed from the smoothed model shown by the red line in (c). (c): representative model of the joint inversion process (blue line) corresponding to appropriate parameterization relevant initial model (black dashed line), and the smoothed model (red line), which is considered the chosen final velocity model. (For interpretation of the references to colour in this figure legend, the reader is referred to the web version of this article.)

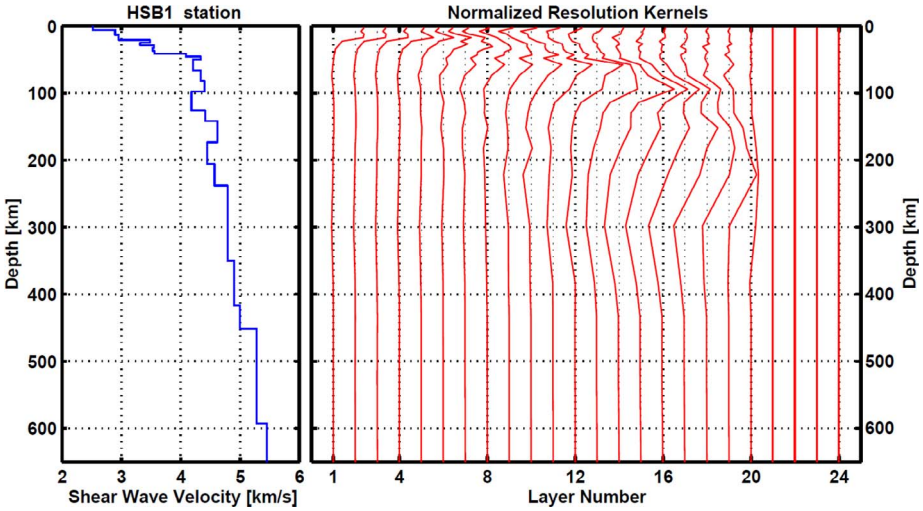

Fig. 7. Chosen final velocity model for station HSB1 (left panel) taken from Fig. 6c-Right. Kernel plots (right panel, with layer number given below) are normalized with respect to the maximum value of the resolution matrix, whose diagonal elements are related to the resolving power, accordingly with Panza (1981).

anomaly is a low velocity/density feature beneath western and central Alborz (the left part of the considered profile corresponds to negative distances from the origin) at a depth range of 50–100 km (Figs. 8 and 9). A low velocity/density anomaly has been reported in a wider area in both lateral and vertical extents by Shad Manaman et al. (2011). Another interesting feature is the zone of high velocity anomalies located at depth range of 100–150 km beneath most of the profile. The Vs and density values in these anomalies are about 4.80 km/s and ~3.60 g/cm^3, respectively; these values are larger than the normal velocity (~4.51 km/s) and density (~3.37 g/cm^3) for the same depth reported by the standard models (e.g., ak135-f, Montagner and Kennett, 1995). Such high velocity features beneath a low velocity anomaly at the upper mantle may explain the major isostatic crustal unbalance previously observed in Alborz (e.g., Dehghani & Makris, 1984; Seber et al., 1997). These features are in favor of the large-scale geodynamic model proposed by Hatzfeld and Molnar (2010) for the Iranian plateau. We develop a similar model for the Alborz Mountains and describe the high velocity/density at depth of 100–150 km as the remnant of mantle lithosphere removed from beneath Alborz. The rise of possibly hotter asthenosphere (shallow low velocity/density feature) following this lithospheric delamination could induce some dynamic buoyancy in the lithosphere beneath the region affected by delamination and cause the rise of the Mountain range even in absence of crustal isostatic compensation.

The free-air gravity anomaly along the Alborz Mountains has distinct values in western (Δg ~360 mGal) and eastern (Δg ~240 mGal)

Table 1
Maximum depth of resolvable features, computed from resolution kernels, and Moho depth defined from the Vs structure beneath each seismic station. The uncertainties are defined as ± half of the incremental step, at the pertinent depth, found by the first regularization step.

Seismic Network	Station Number	Station Name	Longitude [°E]	Latitude [°N]	Maximum Depth of Resolvable Features [km]	Moho Depth [km]
Permanent Stations of IIEES	1	ZNJK	48.6850	36.6700	298	47 ± 2
	2	THKV	50.8790	35.9160	308	50 ± 2
	3	CHTH	51.1260	35.9080	308	47 ± 2
	4	DAMV	51.9710	35.6300	308	50 ± 2
Permanent Stations of IGUT	5	QSDN	49.1740	36.5036	288	42 ± 2
	6	QCNT	50.0091	36.2901	298	42 ± 2
	7	GZV1	50.2183	36.3859	298	50 ± 2
	8	QALM	50.6465	36.4320	294	50 ± 2
	9	HSB1	51.2758	35.4379	294	42 ± 2
	10	TEH1	51.3892	35.7519	291	47 ± 2
	11	ALA1	52.8099	36.0829	298	50 ± 2
Temporary Stations of IIEES	12	DOT1	51.4353	35.4228	288	47 ± 2
	13	TOC1	51.7110	35.5742	288	50 ± 2
	14	CHN1	51.9331	35.4242	298	47 ± 2
	15	AHM1	52.1631	35.4398	298	45 ± 2
	16	ARJ1	52.5123	35.8091	298	42 ± 2
	17	HND1	52.6789	35.7057	298	47 ± 2
	18	MOSB	52.7844	36.2506	308	47 ± 2
	19	ROD1	52.8726	35.9977	298	47 ± 2
	20	SRT1	53.1176	35.9471	298	42 ± 2
	21	GRS1	53.0197	35.7321	294	47 ± 2
	22	ALAB	53.4918	35.5468	308	47 ± 2
	23	FLM1	53.7125	36.0658	298	47 ± 2
	24	JAMB	53.9003	35.7786	298	47 ± 2
	25	GHO1	54.0367	35.9612	298	47 ± 2
	26	TAQ1	54.4288	36.2271	328	47 ± 2

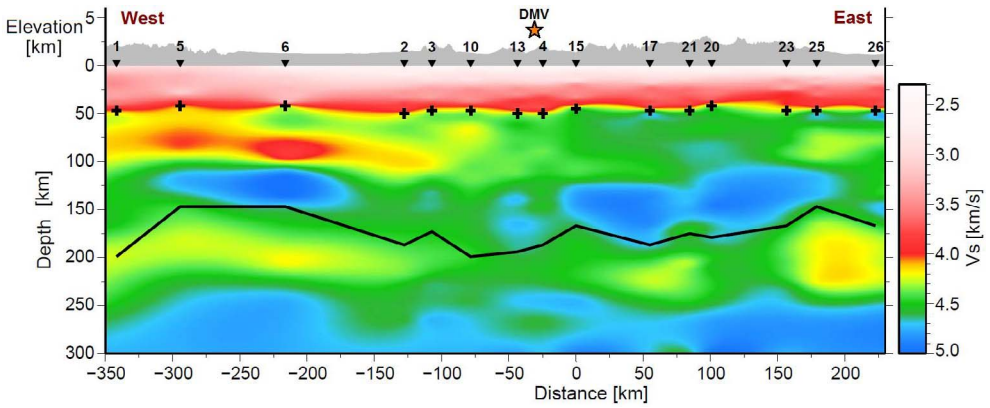

Fig. 8. Vs model along the profile AOA'. The plus symbols and the solid line represent the Moho boundary and LAB, respectively. Elevation variations along the profile are also shown above the velocity model. Star represents the abscissa of the projection of Damavand volcano on the profile AOA′.

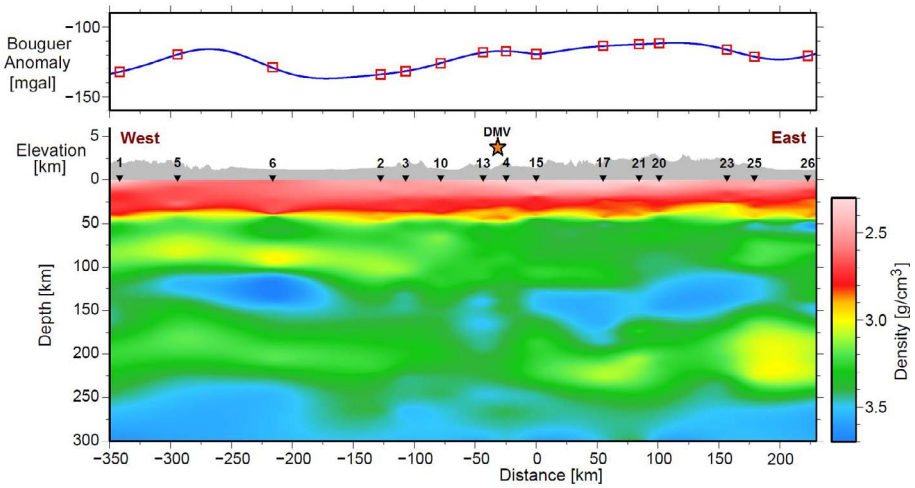

Fig. 9. (Top): observed Bouguer anomaly (blue line) along the profile AOA' as well as predicted Bouguer anomaly (red squares). (Bottom): calculated density distribution with depth along the profile AOA'. Elevation variations along the profile are also shown above the density model. Star represents the abscissa of the projection of Damavand volcano on the profile AOA′. (For interpretation of the references to colour in this figure legend, the reader is referred to the web version of this article.)

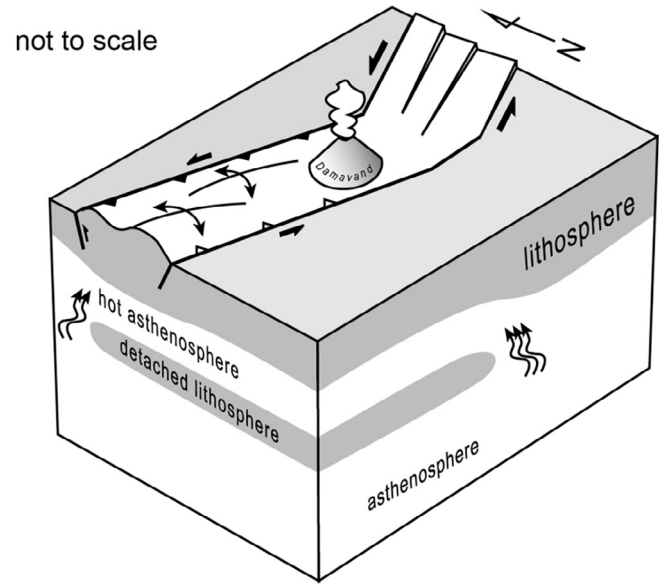

Fig. 10. Simplified sketch illustrating delamination of lower part of western and central Alborz lithosphere (modified after Shabanian et al., 2012). This model is supported by the models presented in Figs. 8 and 9.

portions of Alborz (e.g. see Fig. 11c, Shabanian et al., 2012). Shabanian et al. (2012) have shown that the boundary for the variation in topography and free-air gravity anomalies is NE-SW oriented and that Damavand spot volcano was intruded at this boundary. For Damavand volcano, lithospheric delamination has been proposed as the main cause originating magma production (e.g., Davidson et al., 2004; Liotard et al., 2008). Explaining the especial location of Damavand, Shabanian et al. (2012) proposed a model according which the most compressed and uplifted areas in western and central Alborz correspond with the area where a dense mass has been removed at the base of the lithosphere and it was replaced by hotter asthenosphere; Damavand lies in the easternmost part of the delaminated portion of the range (see their Fig. 13c). They argued that Damavand is located at the junction between two distinct tectonic domains where predominant shortening in the western transpressional regime turns into an eastern transtensional regime, with NE-trending left-lateral faulting (see section 1). Shabanian et al. (2012) concluded that the topography of Alborz reflects kinematics and geometry of its structure in close interaction with lithospheric adjustment.

Our joint inversion results reveal that the shallow low velocity/density anomaly observed at depth range of 50–100 km (Figs. 8, 9 and 10) is clearly limited to western Alborz (the left part of the considered profile corresponding to negative distances from the origin) and well corresponds to the western extent of the lithospheric delamination proposed by Shabanian et al. (2012). This means that the shallow low velocity, interpreted as the raised hotter mantle, is clearly beneath the most contracted and elevated parts of the Alborz Mountains, where the tectonic evolution of the belt had produced suitable conditions for delamination of the lithospheric mantle (Fig. 10).

The geochemical data in Alborz confirm our delamination model for western and central Alborz. They show the existence of enriched mantle source magmatic outcrops in central Alborz, around Damavand (e.g. Liotard et al., 2008), which we consider it as the easternmost part of delaminated portion and in the western Alborz (Nabatian et al., 2016). The geochemical data show that the partial melting has been generated

by a hot shallow upper mantle. This could be an independent evidence supporting delamination hypothesis for western and central Alborz.

6. Concluding remarks

PRFs have been calculated for 26 stations and 1D shear wave velocity models have been derived for each station by joint inversion of PRFs and Rayleigh wave's group velocity data. To validate the resolved S-wave velocity structures, Bouguer anomaly data have been inverted with the geometrical constraint taken from the S-wave velocity models. Our main results are summarized as follow:

The lateral variations in Moho depth along the southern flank of the Alborz Mountains is relatively smooth, with an average depth value of ~47 km. Based on our findings, and on all other reports about crustal thickness for the Alborz Mountain, the average crustal thickness is moderate and it is not enough to compensate the high elevation (average ~2000 m) of the Alborz Mountain.

The resolved velocity and density models show a heterogeneous upper mantle beneath the Alborz Mountains, well consistent with the difference in the free-air gravity anomalies in eastern and western parts of the Mountain range. The high velocity/density feature observed beneath the whole Mountain range, between 100 and 150 km depths, is likely the expression of lithospheric delamination under the belt. On the other side, the low velocity/density feature, in the depth range of 50–100 km, is only observed beneath the western and central portions of Alborz; this anomaly is absent beneath the eastern part of the belt. These observations may imply the occurrence of a mature delamination process in western Alborz consistent with its distinct tectonic configuration. The delamination process is suggested to be responsible for major isostatic crustal unbalance and abnormal uprise of the Alborz Mountain range.

Acknowledgements

We specially appreciate the Editor, Vernon Cormier, and two anonymous reviewers for their constructive comments. We thank Prof. Robert Herrmann for providing the receiver function/surface wave inversion routine. We acknowledge the Iranian Seismological Center (IRSC) and International Institute of Earthquake Engineering and Seismology (IIEES) for providing the required waveforms for this study. The article was supported by the Iranian National Science Foundation (grant number 92008225) and partially by Italian MIUR (PRIN 2015 project).

References

Allen, M.B., Ghassemi, M.R., Sharabi, M., Qoraishi, M., 2003. Accommodation of late Cenozoic oblique shortening in the Alborz range, northern Iran. J. Struct. Geol. 25, 659–672.

Ashtari, M., Hatzfeld, D., Kamalian, N., 2005. Microseismicity in the region of Tehran. Tectonophysics 395 (3–4), 193–208.

Berberian, M., Qorashi, M., Arzhangravesh, B., Mohajer-Ashjai, A., 1983. Recent tectonics, seismotectonics and earthquake-fault hazard study in the greater Tehran region. Geol. Surv. Iran 56, 130p (In Persian).

Brune, J., Dorman, J., 1963. Seismic waves and earth structure in the Canadian Shield. Bull. seism. Soc. Am. 53, 167–210.

Chen, L., Jiang, M., Talebian, M., Ghods, A., Chung, S.L., Ai, Y., Sobouti, F., He, Y., Motaghi, K., Zheng, T., Faridi, M., 2016. New seismic array observation in the Northwestern Iranian Plateau. EGU General Assembly Conference Abstracts, vol. 18, 3427.

Davidson, J.P., Hassanzadeh, J., Berzins, R., Stockli, D.F., Bashukooh, B., Turrin, B., Pandamouz, A., 2004. The geology of Damavand volcano, Alborz Mountains, northern Iran. Geol. Soc. Am. Bull. 116, 16–29. http://dx.doi.org/10.1130/B25344.1.

Dehghani, G., Makris, J., 1984. The gravity field and crustal structure of Iran, Neues Jahrb. Geol. Palaeontol. Abh. 168, 215–229.

Djamour, Y., Vernant, P., Bayer, R., Nankali, H., Ritz, J.F., Hinderer, J., Hatam, Y., Luck, B., Le Moigne, N., Sedighi, M., Khorrami, F., 2010. GPS and gravity constraints on continental deformation in the Alborz Mountain range, Iran. Geophys. J. Int. 183, 1287–1301.

Dziewonski, A.M., Anderson, D.L., 1981. Preliminary reference Earth model. Phys. Earth Planet. Inter. 25, 297–356.

Gonzalez, O., Moreno, B., Romanelli, F., Panza, G.F., 2012. Lithospheric structure below seismic stations in Cuba from the joint inversion of Rayleigh surface waves dispersion and receiver functions. Geophys. J. Int. 189, 1047–1059.

Hatzfeld, D., Molnar, P., 2010. Comparisons of the kinematics and deep structures of the Zagros and Himalaya and of the Iranian and Tibetan plateaus and geodynamic implications. Rev. Geophys. 48. http://dx.doi.org/10.1029/2009RG000304.

Hedayati, A., Brander, J.L., Berberian, M., 1976. Microearthquake survey of Tehran region, Iran. Bull. Seismol. Soc. Am. 66, 1713–1725.

Herrmann, R.B., 2013. Computer programs in seismology: an evolving tool for instruction and research. Seism. Res. Lett. 84, 1081–1088. http://dx.doi.org/10.1785/0220110096.

Hessami, K., Jamali, F., Tabassi, H., 2003. Major Active Faults of Iran (map), scale 1:2, 500,000; Ministry of Science, Research and Technology, International Institute of Earthquake Engineering and Seismology.

Jackson, J., Priestley, K., Allen, M., Berberian, M., 2002. Active tectonics of the South Caspian Basin. Geophys. J. Int. 148, 214–245.

Julia, J., Ammon, C.J., Herrmann, R.B., Correig, A.M., 2000. Joint inversion of receiver function and surface wave dispersion observations. Geophys. J. Int. 143, 1–19.

Kind, R., Vinnik, L.P., 1988. The upper mantle discontinuities underneath the GRF array from P-to-S converted phases. J. Geophys. 62, 138–147.

Last, R.J., Nyblade, A.A., Langston, C.A., Owens, T.J., 1997. Crustal structure of the East African Plateau from receiver functions and Rayleigh wave phase velocities. J. Geophys. Res. 102, 24469–24483.

Ligorria, J.P., Ammon, C.J., 1999. Iterative deconvolution and receiver-function estimation. Bull. Seismol. Soc. Am. 89 (5), 1395–1400.

Liotard, J.M., Dautria, J.M., Bosch, D., Condomines, M., Mehdizadeh, M., Ritz, J.-F., 2008. Origin of the absarokite–banakite association of the Damavand volcano (Iran): trace elements and Sr, Nd, Pb isotope constraints. Int. J. Earth Sci. 97, 89–102. http://dx.doi.org/10.1007/s00531-006-0159-6.

Ludwig, W.J., Nafe, J.E., Drake, C.L., 1970. Seismic Refraction. Wiley InterScience, New York.

Menke, W., 1989. Geophysical Data Analysis: Discrete Inverse Theory. Academic Press Inc, New York.

Montagner, J.P., Kennett, B.L.N., 1995. How to reconcile body-wave and normal-mode reference Earth models? Geophys. J. Int. 125, 229–248.

Motaghi, K., Tatar, M., Priestley, K., 2012. Crustal thickness variation across the northeast Iran continental collision zone from teleseismic converted waves. J. Seismol. 16 (2), 253–260.

Motaghi, K., Tatar, M., Priestley, K., Romanelli, R., Doglioni, C., Panza, G.F., 2015. The deep structure of the Iranian Plateau. Gondwana Res. 28 (1), 407–418.

Motaghi, K., Shabanian, E., Kalvandi, F., 2017. Underplating along the northern portion of the Zagros suture zone, Iran. Geophys. J. Int. 210 (1), 375–389.

Nabatian, G., Jiang, S.Y., Honarmand, M., Neubauer, F., 2016. Zircon U-Pb ages, geochemical and Sr–Nd–Pb–Hf isotopic constraints on petrogenesis of the Tarom-Olya pluton, Alborz magmatic belt, NW Iran. Lithos 244, 43–58.

Nemati, M., Hatzfeld, D., Gheitanchi, M., Sadidkhouy, A., Mirzaei, N., 2011. Microseismicity of the Astane-Firouzkuh faults, east Alborz, Iran. Tectonophysics 506 (1–4), 11–21.

Panza, G.F., 1981. The resolving power of seismic surface waves with respect to crust and upper mantle structural models. Plenum Publ. Corp., pp. 39–77.

Panahi Vaghar, C., Voosoghi, B., Haji Aghajani, S., 2017. Digital Terrain Model (DTM) of the North Alborz region based on its underneath faulting. J. Earth Space Phys. 43 (2), 229–245 (in Persian).

Radjaee, A.H., Rham, D., Mokhtari, M., Tatar, M., Priestley, K., Hatzfeld, D., 2010. Variation of Moho depth in the central part of the Alborz Mountains, northern Iran. Geophys. J. Int. 181 (1), 173–184.

Rahimi, H., Hamzehloo, H., Vaccari, F., Panza, G.F., 2014. Shear-wave velocity tomography of the lithosphere-asthenosphere system beneath the Iranian Plateau. Bull. Seismol. Soc. Am. 104 (6), 2782–2798.

Ries, J., Bettadpur, S., Eanes, R., Kang, Z., Ko, U., McCullough, C., Nagel, P., Pie, N., Poole, S., Richter, T., Save, H., Tapley, B., 2016. The Combination Global Gravity Model GGM05C. University of Texas, Austin, Texas.

Ritz, J.-F., Nazari, H., Ghassemi, A., Salamati, R., Shafei, A., Solaymani, S., Vernant, P., 2006. Active transtension inside Central Alborz: a new insight into the northern Iran-southern Caspian geodynamics. Geology 34 (6), 477–480.

Seber, D., Vallve, M., Sandvol, E., Steer, D., Barazangi, M., 1997. Middle East tectonics: applications of geographic information systems (GIS). GSA Today 7 (2), 1–6.

Shabanian, E., Acocella, V., Gioncada, A., Ghasemi, H., Bellier, O., 2012. Structural control on volcanism in intraplate post collisional settings: late cenozoic to quaternary examples of Iran and Eastern Turkey. Tectonics 31, TC3013. http://dx.doi.org/10.1029/2011TC003042.

Shad Manaman, N., Shomali, H., Koyi, H., 2011. New constraints on upper-mantle S-velocity structure and crustal thickness of the Iranian plateau using partitioned waveform inversion. Geophys. J. Int. 184, 247–267.

Sodoudi, F., Yuan, X., Kind, R., Heit, B., Sadidkhouy, A., 2009. Evidence for a missing crustal root and a thin lithosphere beneath the Central Alborz by receiver function studies. Geophys. J. Int. 177 (2), 733–742.

Solaymani Azad, S., Ritz, J.F., Abbassi, M.R., 2011. Left-lateral active deformation along the Mosha-North Tehran fault system (Iran): morphotectonics and paleoseismological investigations. Tectonophysics 497, 1–14.

Trifonov, V.G., Hessami, K.T. and Jamali, F., 1996, West-Trending Oblique Sinitral–Reverse Fault system in Northern Iran, IIEES Special Pub., No. 75-96-2, Tehran, Iran.

Urban, L., Cichowicz, A., Vaccari, F., 1993. Computation of analytical partial derivatives of phase and group velocities for Rayleigh waves with respect to structural parameters. Studia Geoph. et Geod. 37, 14–36.

USGS catalog, 2015. United States Geological Survey, On-line Bulletin, http://www.usgs.gov.

Vernant, P., Nilforoushan, F., Hatzfeld, D., Abbasid, M.R., Vigny, C., Masson, F., Nankali, H., Martinod, J., Ashtiani, A., Bayer, R., Tavakoli, F., Chery, J., 2004. Present-day crustal deformation and plate kinematics in the Middle East constrained by GPS measurements in Iran and northern Oman. Geophys. J. Int. 157, 381–398.

Zhu, L.P., Kanamori, H., 2000. Moho depth variation in southern California from teleseismic receiver functions. J. Geophys. Res. 105, 2969–2980.